

MaGICC-WDM: the effects of warm dark matter in hydrodynamical simulations of disc galaxy formation

Jakob Herpich^{1*}, Gregory S. Stinson¹, Andrea V. Macciò¹, Chris Brook², James Wadsley³, Hugh M. P. Couchman³, Tom Quinn⁴

¹*Max-Planck-Institut für Astronomie, Königstuhl 17, D-69117 Heidelberg, Germany*

²*Departamento de Física Teórica, Universidad Autónoma de Madrid, E-28049 Cantoblanco, Madrid, Spain*

³*Department of Physics and Astronomy, McMaster University, Hamilton, Ontario L8S 4M1, Canada*

⁴*Astronomy Department, University of Washington, Box 351580, Seattle, WA 98195-1580, USA*

27 November 2021

ABSTRACT

We study the effect of warm dark matter (WDM) on hydrodynamic simulations of galaxy formation as part of the Making Galaxies in a Cosmological Context (MaGICC) project. We simulate three different galaxies using three WDM candidates of 1, 2 and 5 keV and compare results with pure cold dark matter simulations. WDM slightly reduces star formation and produces less centrally concentrated stellar profiles. These effects are most evident for the 1 keV candidate but almost disappear for $m_{\text{WDM}} > 2$ keV. All simulations form similar stellar discs independent of WDM particle mass. In particular, the disc scale length does not change when WDM is considered. The reduced amount of star formation in the case of 1 keV particles is due to the effects of WDM on merging satellites which are on average less concentrated and less gas rich. The altered satellites cause a reduced starburst during mergers because they trigger weaker disc instabilities in the main galaxy. Nevertheless we show that disc galaxy evolution is much more sensitive to stellar feedback than it is to WDM candidate mass. Overall we find that WDM, especially when restricted to current observational constraints ($m_{\text{WDM}} > 2$ keV), has a minor impact on disc galaxy formation.

Key words: hydrodynamics – methods: numerical – galaxies: formation – galaxies: spiral – cosmology: dark matter

1 INTRODUCTION

In the cold dark matter (CDM) framework, dark matter (DM) is composed of massive particles that interact only gravitationally. Due to their mass, cold dark matter particles have a negligible velocity dispersion when they decouple from the primordial plasma, so they are dynamically cold.

Results of numerical N -body simulations of structure formation in the Universe based on the CDM model are in excellent agreement with observations of the large-scale structure of the Universe, such as the observed clustering of galaxies (e.g. Springel et al. 2005).

Despite this remarkable success, predictions of the CDM model based on collisionless simulations seem to contradict observations on galactic and sub-galactic scales. CDM-based simulations predict ~ 50 times as many satellites for Milky Way (MW) mass DM haloes than can be found orbiting the

MW (Moore et al. 1999). Klypin et al. (1999) found a similar result for the MW and Andromeda galaxies. Whereas CDM predicts that satellite mass functions are self-similar between different halo masses, observed satellite luminosity functions vary a lot as a function of the mass of the central object (e.g. Diemand et al. 2004). This discrepancy constitutes the *Missing-Satellites problem*. Other studies have considered baryonic processes like cosmic reionization and stellar feedback and found that they limit gas cooling into small satellites, making them either too dim to be observed or completely dark (e.g. Efstathiou 1992; Quinn et al. 1996; Bullock et al. 2000; Somerville 2002; Koposov et al. 2009; Okamoto & Frenk 2009; Macciò et al. 2010b; Font et al. 2011; Nickerson et al. 2011).

Boylan-Kolchin et al. (2011) showed that not only the number of observed satellites but also their mass profiles are inconsistent with the collisionless CDM prediction. The 10 satellites most massive at the time of accretion in the Aquarius simulations (Springel et al. 2008) have rotation curves

* Email: herpich@mpia.de

that rise more steeply than the observed rotation velocity of the 10 most luminous satellites in the MW halo. These satellites are ‘too big to fail’; their analogues should form dwarf galaxies sufficiently luminous to be observed in the MW. It remains unclear whether baryons can alter the DM density profiles enough in such small objects to solve this problem (e.g. Zolotov et al. 2012; Garrison-Kimmel et al. 2013).

Due to these shortcomings of CDM, alternative DM particles have been suggested. One possible particle species is a thermal relic warm dark matter (WDM). Such WDM particles decouple much earlier than CDM particles due to their lower mass (keV scale for WDM versus GeV and higher for CDM). Thus, the WDM particles have a non-negligible velocity dispersion at the time of decoupling. Due to their velocity dispersion, WDM particles can escape from shallow potential wells and diffuse into underdense regions so that small-scale density perturbations are reduced instead of amplified. The particle diffusion is called *free streaming* and causes the WDM power spectrum to be suppressed on small scales (i.e. large k). As a result, structure formation takes longer in WDM models compared to CDM on all scales, and the amount of substructure on small scales is suppressed (e.g. Colín et al. 2000; Bode et al. 2001; Knebe et al. 2002; Gao & Theuns 2007; Kuzio de Naray et al. 2010; Schneider et al. 2012). At the same time surviving substructures have rotation curves in better agreement with observations (Lovell et al. 2012; Anderhalden et al. 2013).

Thermal relic WDM particles are only one possible WDM particle family. There are many other WDM candidates including sterile neutrino and gravitinos (Hansen et al. 2002; Abazajian & Koushiappas 2006; Boyarsky et al. 2009a). There is a one-to-one relation between sterile neutrino mass and thermal relic candidate mass, however, so it is always possible to recast constraints for a thermal candidate in terms of a sterile neutrino mass (Colombi et al. 1996). Other more complex models have been extensively discussed in the literature, like mixed models (e.g. Boyarsky et al. 2009a; Macciò et al. 2013) or composite DM models (Khlopov & Stephan 2005; Khlopov & Kouvaris 2008).

Observational results have ruled out the most extreme WDM candidates. Early measurements of the Lyman- α forest in spectra of quasi-stellar objects (QSOs) implied a lower limit on the mass of WDM thermal relic particles of $m_{\text{WDM}} \gtrsim 1 \text{ keV}$ (Narayanan et al. 2000; Hansen et al. 2002; Viel et al. 2005, 2006, 2008; Seljak et al. 2006; Boyarsky et al. 2009b). Fluxes from gravitationally lensed QSOs (Miranda & Macciò 2007) and the distribution of satellites in the MW (Macciò & Fontanot 2010a) provide similar constraints. The most recent study of high redshift quasars’ flux power spectra (Viel et al. 2013) tightened the constraints further to exclude WDM candidate masses below 3.3 keV at a confidence level of 2σ .

So far most of the studies focusing on the effect of WDM on galaxy formation have been based on pure DM simulations (e.g. Schneider et al. 2012, and references therein) or combine collisionless simulations with semi-analytical models of galaxy formation (Macciò & Fontanot 2010a; Menci et al. 2012, 2013; Kang et al. 2013).

So far, though, one of the most powerful tools for studying galaxy formation and evolution in a cosmological context, high resolution hydrodynamical simulations, have yet

to consider WDM. Recently, several groups have been able to form realistic looking disc galaxies simulated in a CDM universe over a wide mass range (Robertson et al. 2006; Governato et al. 2007; Agertz et al. 2011; Guedes et al. 2011; Brook et al. 2012; Scannapieco et al. 2012; Marinacci et al. 2013; Stinson et al. 2013a).

In this study, we aim to fill this gap by combining high resolution hydrodynamical simulations with WDM-based cosmological models. This study is part of the Making Galaxies in a Cosmological Context (MaGICC) project, a large simulation campaign aiming to unveil the process of galaxy formation in a Universe ruled by DM (and dark energy).

Simulations performed within the MaGICC project in a CDM scenario have been successful in reproducing many observations of galaxies. The simulations follow both the $z = 0$ and the redshift evolution of the stellar to halo mass relation (e.g. Moster et al. 2010, 2013) as detailed in Stinson et al. (2013a). They reproduce the distribution of metals (e.g. O VI) around star-forming galaxies (Stinson et al. 2012) and create galaxy rotation curves in agreement with observations (Macciò et al. 2012b; Di Cintio et al. 2013). They form discs with an old, thick component and a young, thin component that match the chemical patterns observed in the MW (Stinson et al. 2013b).

In this work, we resimulate three galaxies introduced in the McMaster Unbiased Galaxy Simulations (MUGS) project (Stinson et al. 2010) using various thermal WDM models (5, 2 and 1 keV) to assess the impact of WDM on galaxy properties. The paper is organized as follows. §2 describes the simulations that were used for this comparison. §3 details the main properties of the simulated galaxies and §4 presents our conclusions.

2 SIMULATIONS

The three galaxies from the MUGS project are g1536, g5664 and g15784 (for details see Stinson et al. 2010). The galaxies are simulated in a periodic box $50 h^{-1} \text{ Mpc}$ on a side from redshift $z = 99$. The simulation parameters are consistent with a *Wilkinson Microwave Anisotropy Probe* 3 cosmology ($H_0 = 73 \text{ km s}^{-1} \text{ Mpc}^{-1}$, $\Omega_m = 0.24$, $\Omega_b = 0.04$, $\Omega_l = 0.76$, $\Omega_b = 0.04$, $\sigma_8 = 0.76$ Spergel et al. 2007). Each galaxy is simulated using three different WDM models: $m_{\text{WDM}} = 5 \text{ keV}$ (WDM5), 2 keV (WDM2), 1 keV (WDM1) and, for reference, one realization of a standard CDM model. Initial conditions were created with and without baryons with identical resolution. The DM particle mass is $1.1 \times 10^6 M_\odot$, the initial gas particle mass is $2.2 \times 10^5 M_\odot$ and the initial star particle mass is $6.3 \times 10^4 M_\odot$. All the properties of the different galaxies with baryons are summarized in Table 1.

2.1 Initial conditions

For the CDM simulations we used the initial conditions files from the MUGS project. New initial conditions were created for each WDM model from the same region of space as every MUGS galaxy. The WDM initial condition creation is identical to the CDM model (Stinson et al. 2010) except for a modified initial DM power spectrum. The same random

Table 1. A summary of the properties of simulated galaxies, that includes the virial (M_{200}), stellar (M_*), gas (M_{gas}) and total baryonic mass (M_{bary}) as well as the virial radius (R_{200}). Note that only the results for those simulations including baryons are presented.

Galaxy	Model	m_{WDM} (keV)	M_{200} ($10^{10} M_{\odot}$)	M_* ($10^{10} M_{\odot}$)	M_{gas} ($10^{10} M_{\odot}$)	M_{bary} ($10^{10} M_{\odot}$)	R_{200} (kpc)
g1536	CDM	∞	56	2.4	4.9	7.3	166
g1536	WDM5	5	56	2.1	4.8	6.9	165
g1536	WDM2	2	56	1.8	5.0	6.8	165
g1536	WDM1	1	55	1.5	5.0	6.5	165
g5664	CDM	∞	44	2.7	3.1	5.8	153
g5664	WDM5	5	44	2.3	3.1	5.5	152
g5664	WDM2	2	45	2.7	3.3	5.9	154
g5664	WDM1	1	39	0.7	3.9	4.5	148
g15784	CDM	∞	121	8.3	9.5	17.8	214
g15784	WDM5	5	123	7.9	9.1	17.0	215
g15784	WDM2	2	121	8.2	9.2	17.3	213
g15784	WDM1	1	119	8.9	9.0	18.0	213

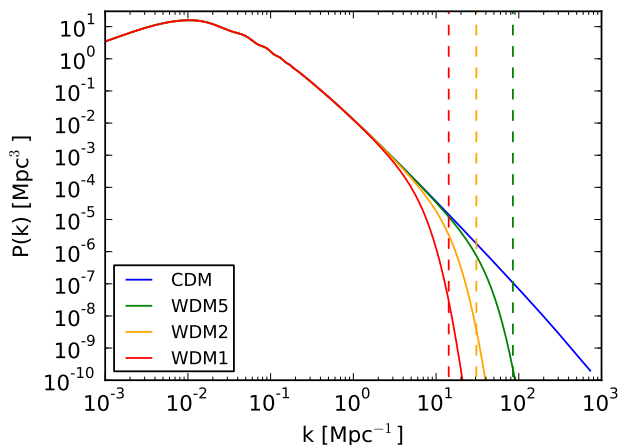


Figure 1. WDM power spectra. The figure shows the power spectra at $z = 99$ for all simulated DM candidates. The blue, green, yellow and red lines correspond to CDM, WDM5, WDM2 and WDM1, respectively. The vertical dashed lines indicate the scale of the break in the WDM power spectra α . The figure shows the suppression of power at large k in the WDM initial conditions. These power spectra are used to sample initial conditions.

seed was used for the generation of both warm and CDM initial conditions.

The WDM power spectra are computed using a ‘relative transfer function’ to the CDM power spectrum as in Bode et al. (2001):

$$P_{\text{WDM}}(k) = [T_{\text{WDM}}(k)]^2 P_{\text{CDM}}(k), \quad (1)$$

with

$$T(k) = [1 + (\alpha k)^{2\nu}]^{-5/\nu}, \quad (2)$$

where α is the length-scale of the break in the WDM power spectrum. Viel et al. (2005) found $\nu = 1.12$ and

$$\alpha = 0.049 \left(\frac{m_{\text{WDM}}}{1 \text{ keV}} \right)^{-1.11} \left(\frac{\Omega_{\text{WDM}}}{0.025} \right)^{0.11} \left(\frac{h}{0.7} \right)^{1.22} h^{-1} \text{Mpc}. \quad (3)$$

Fig. 1 shows the initial power spectra at $z = 99$ for all simulated DM candidates. From the figure, it is evident that power on small spatial scales (large k) is suppressed for warmer DM candidates. Given the mass resolution of

the simulation and the choice of WDM models, the contribution from WDM velocity dispersion is ignored since it is less than 1% of the initial Zel’dovich velocity (Macciò et al. 2012a). Therefore, only the WDM modification to the power spectrum is considered.

2.2 Hydrodynamics

The simulations use the smoothed particle hydrodynamics code GASOLINE (Wadsley et al. 2004). It includes metallicity-dependent gas cooling, star formation (SF) and a detailed chemical enrichment model. The physics used in the MaGICC project is detailed in Stinson et al. (2013a). Briefly, stars are formed from gas cooler than $T_{\text{max}} = 1.5 \times 10^4$ K and denser than 9.3 cm^{-3} according to the Kennicutt-Schmidt law (Kennicutt 1998) as described in Stinson et al. (2006) with a star formation efficiency (SFE) parameter $c_* = 0.1$. The SF density threshold is then set to the maximum density at which gravitational instabilities can be resolved, $32 M_{\text{gas}} \epsilon^{-3} (n_{\text{th}} > 9.3 \text{ cm}^{-3})$, where $M_{\text{gas}} = 2.2 \times 10^5 M_{\odot}$ and ϵ is the gravitational softening (310 pc).

The star particles are $6.3 \times 10^4 M_{\odot}$, massive enough to represent an entire stellar population consisting of stars with masses given by the Chabrier (2003) initial mass function. 20% of these have masses greater than $8 M_{\odot}$ and explode as Type II supernovae (SNeII) from 3.5 until 35 Myr after the star forms, based on the Padova stellar lifetimes (Alongi et al. 1993; Bressan et al. 1993). Each supernova (SN) inputs $E_{\text{SN}} = 10^{51}$ erg of purely thermal energy into the surrounding gas. This energy would be radiated away before it had any dynamical impact because of the high density of the star forming gas (Katz 1992). Thus, the SN feedback relies on temporarily delaying cooling based on the subgrid approximation of a blastwave as described in Stinson et al. (2006).

The SNe feedback does not start until 3.5 Myr after the first massive star forms. However, nearby molecular clouds show evidence of being blown apart *before* any SNeII have exploded. Pellegrini et al. (2007) emphasized the energy input from stellar winds and ultraviolet (UV) radiation pressure in M17 prior to any SNeII explosions. Lopez et al. (2011) found similar energy input into 30 Doradus. Thus, in the time period before SNe start exploding, we distribute 10% of the luminosity produced in the stellar population, an

amount equivalent to the UV luminosity, to the surrounding gas without disabling the cooling. Following the convention of Stinson et al. (2013a), we call this feedback from massive stars: ‘Early Stellar Feedback’ (ESF). Most of the energy coming from the ESF is immediately radiated away, but Stinson et al. (2013a) have shown that this ESF has a significant effect on the star formation history (SFH) of a MW mass galaxy and places the halo on the Moster et al. (2013) stellar mass–halo mass relationship at $z = 0$.

To test how the impact of WDM compares with the effect of stellar feedback, we ran an additional suite of simulations of the $m_{\text{WDM}} = 1 \text{ keV}$ initial conditions with a range of reduced ESF efficiencies. A summary of these galaxies’ properties is given in Table 2.

2.3 Halo identification

The Amiga Halo Finder (Knollmann & Knebe 2009) identifies all the bound particles in the simulated galaxies. The virial overdensity was chosen to be 200, so that the virial radius and virial mass are R_{200} and M_{200} , respectively. The centre for all profile plots was calculated using the shrinking sphere algorithm (Power et al. 2003). To track the evolution of certain properties of the simulated galaxies the most massive progenitor at $z = 4.5$ has been identified and traced up to $z = 0$.

3 RESULTS

We first examine the basic properties of the galaxies as a function of DM candidate mass. We then re-examine those properties for the WDM1 case, in runs performed with different stellar feedback parametrization.

3.1 From cold to warm

Fig. 2 shows mock observational images of the simulated galaxy g1536 at $z = 0$ in the two extreme DM models: CDM and WDM1. The images are 50 kpc on a side. They were created using the radiative transfer code SUNRISE (Jonsson 2006). Both images show signs of spiral patterns of young stars (blue) with the CDM simulation showing perhaps more structured spiral arms. The WDM1 simulation has a notably reduced stellar density in the centre compared to the CDM simulation. The edge-on view (bottom panels) shows that the stars are assembled in a disc in both cases.

Fig. 3 shows DM density profiles of all realizations of g1536 with (right-hand panel) and without (left-hand panel) baryonic physics. In the simulations without baryons, all DM models yield the same DM density profile. This is consistent with previous studies of the concentration–mass relation in WDM models at the scale of massive disc galaxies (Schneider et al. 2012). In simulations using baryonic physics, the DM density profiles in the centre are steeper for colder DM models. As we will show, these steeper profiles are due to the dynamical effects of increased SF in the centre of the CDM simulations of g1536. The results are consistent with the recent study by Di Cintio et al. (2013), which has shown that for a galaxy at the peak of the SFE, the effect of baryons is to mildly contract the DM density profile.

The slightly steeper density profiles are also reflected in

the rotation curves (left-hand panel of Fig. 5) and surface brightness profiles (left-hand panel of Fig. 6) of g1536. This suggests that WDM has no direct effect on the DM distribution of the simulated halo. Instead, they are a secondary consequence of the effect of WDM on SF in the galactic disc.

3.1.1 Stellar mass–halo mass relationship

In the MaGICC project, the main constraint is the stellar mass–halo mass relation (e.g. Moster et al. 2013, hereafter called *Moster relation*). Therefore, we first compare all simulated galaxies with this fundamental relationship.

The upper-left panel of Fig. 4 shows the stellar mass of all galaxies as a function of their halo mass at $z = 0$. All simulations of the g1536 galaxy (star symbols) fall within the expected variation in the relationship. While all DM models yield the same halo mass ($\approx 6 \times 10^{11} M_{\odot}$), there is a trend towards lower stellar masses with decreasing values for m_{WDM} .

Each of the other three panels of Fig. 4 show how the stellar mass to halo mass ratio varies as a function of time for each galaxy individually. The black line shows the evolution based on the stellar mass predicted using the Moster relation with the evolution of the halo mass. The grey region represents the 1σ variation in this measurement. The upper-right panel shows the results for all realizations of g1536. It shows that the trend of reduced stellar content of the galaxy in WDM starts at $z \approx 1$. From this panel, we also see that every realization of g1536 evolves consistently with the Moster relation at all times.

g5664 is denoted with circles in Fig. 4. At $z = 0$ (upper-left panel) the CDM, WDM5 and WDM2 galaxies have the same halo mass ($\approx 4.5 \times 10^{11} M_{\odot}$) and almost the same stellar mass. Their stellar mass is above the expected value but remains marginally consistent with the scatter. The WDM1 galaxy is slightly less massive in halo mass and has dramatically fewer stars. Its stellar content falls below the expected Moster relation variation at $z = 0$. All simulations of g5664 evolve consistently with the Moster relation until $z < 1$ (lower-left panel) but while the CDM, WDM5 and WDM2 models all sharply increase their stellar mass, the WDM1 model forms far fewer stars from $z \approx 3$.

Looking at the other WDM models, the clear trend of decreasing stellar mass with warmer DM models at $z \lesssim 1$ in g1536 does not happen in g5664. The CDM model still forms the most stars, but the WDM2 simulation forms more stars than the WDM5 model.

All simulations of the g15784 galaxy have about the same halo mass ($M_{200} > 10^{12} M_{\odot}$), but form more stars than are expected from the Moster relation (squares in upper-left panel of Fig. 4). The stellar mass–halo mass ratios of g15784 evolve along similar trajectories for all the initial conditions (lower-right panel). Their stellar mass increases far above the expected variance at $z = 2$. The increase is due to an extended SF event that cannot be halted by any of the feedback processes that are included in our simulations (for other examples, see Kannan et al. 2013).

The case of g15784 illustrates that any effects that WDM may have on galaxy formation are dwarfed by the problem of overcooling in the mass regime of $M_{200} \gtrsim 10^{12} M_{\odot}$. Thus, for our study of the effect of WDM on galaxy formation, it is unnecessary for us to consider this galaxy for

Table 2. A summary of the properties of simulated representations of g1536 with reduced ESF in the WDM1 model, that includes the virial (M_{200}), stellar (M_*), gas (M_{gas}) and total baryonic mass (M_{bary}) as well as the virial radius (R_{200}). Note that only the results for those simulations including baryons are presented.

Label	c_{ESF} (%)	M_{200} ($10^{10} M_{\odot}$)	M_* ($10^{10} M_{\odot}$)	M_{gas} ($10^{10} M_{\odot}$)	M_{bary} ($10^{10} M_{\odot}$)	R_{200} (kpc)
ESF 10	10	55	1.5	5.0	6.5	165
ESF 7.5	7.5	59	3.6	4.6	8.1	168
ESF 5	5	60	4.2	4.6	8.8	170
ESF 1	1	59	3.4	4.7	8.2	168
ESF 0	0	57	2.8	4.6	7.3	167

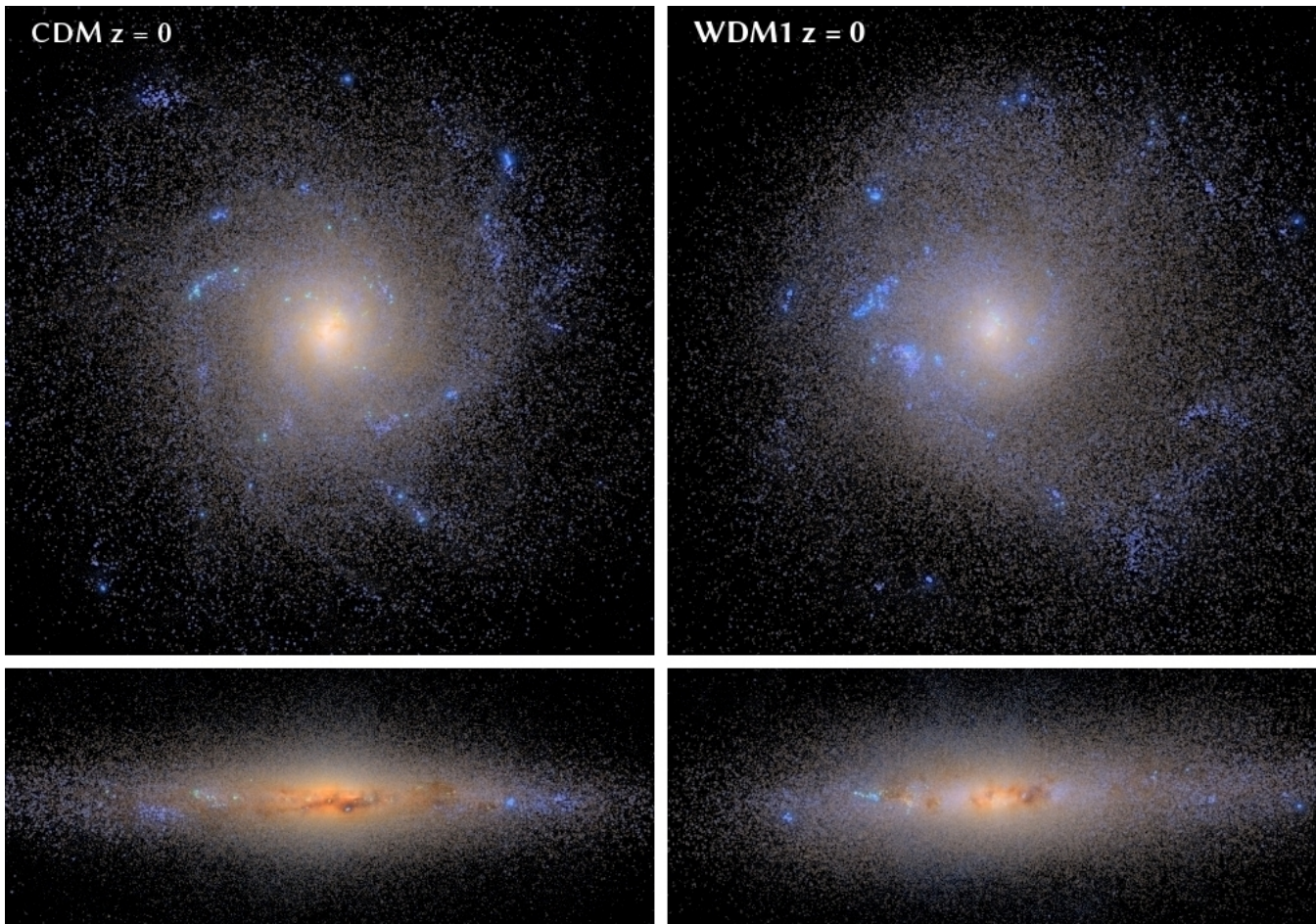


Figure 2. Face-on (upper panel) and edge-on (lower panel) images of the simulated galaxy g1536 at $z = 0$. Each panel is 50 kpc on a side. The left-hand panel shows the CDM simulation while the right-hand panel shows the WDM1 simulation. The images were created using the Monte Carlo radiative transfer code SUNRISE. Brightness and contrast in the image are scaled as $a \sin h$ as described in Lupton et al. (2004).

further analysis. The behaviour of g15784 also helps illustrate the need to use *realistic* galaxies to study the effect of any variation of the cosmological parameters, whether it be the properties of DM or dark energy. Overcooling is a common problem in simulations, and its effects can overshadow the effects of cosmology.

3.1.2 Mass distribution

Fig. 5 shows circular velocities $v_c = \sqrt{GM(R)/R}$ as a function of radius R of the g1536 (left-hand panel) and

g5664 (right-hand panel) galaxies (solid lines). The total rotation curve is split into the individual contributions from DM (dashed), stellar (dotted) and gas (dash-dotted) mass $M(< R)$. All rotation curves for g1536 are either flat or slowly rising. Warmer DM models (i. e. decreasing m_{WDM}) have lower maximum rotation velocities and are more slowly rising.

The rotation curve for the CDM model for g5664 has a central peak as we would expect based on its high rate of SF. The central peak is less pronounced in the WDM simulations, and the WDM1 model that formed too few stars has

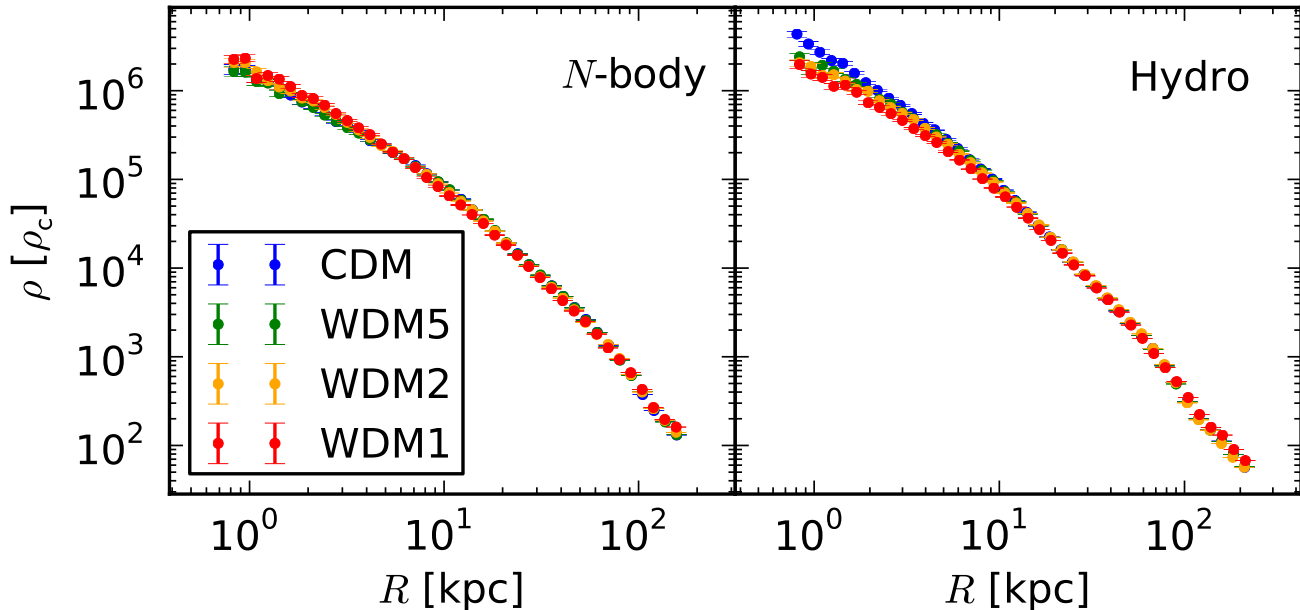


Figure 3. DM density profiles of all simulations of the g1536 galaxy. The left-hand panel shows the density profiles of the pure N -body simulations, the right-hand panel shows the results for the hydrodynamic simulations. The blue, green, yellow and red points correspond to the CDM, WDM5, WDM2 and WDM1 models, respectively. The radial range is $2.5\epsilon < R < R_{200}$. There is no significant influence of the nature of DM on its density profile in N -body simulations. However, baryonic physics may alter the central DM profile as the right-hand panel shows.

a slowly rising rotation curve. Like for the SF, the rotation curves of the WDM2 and WDM5 are in the opposite order in g5664 from what they are in g1536.

For both galaxies, the contributions to the rotation curves from DM and gas are quite similar between the different DM models. The largest difference in contribution to the rotation curve comes from the stars in the central 5 kpc. Thus, the difference in stellar masses apparent in Fig. 4 results from excess SF in the centre of the galaxies, rather than stars accreted from satellites.

Another, more directly observable, way to look at the mass distribution in our simulated galaxies is the B -band surface brightness profiles shown in Fig. 6. Again, the left-hand panel shows data for g1536 and the right-hand panel for g5664. Except for the WDM1 simulation of g5664, all galaxies feature an exponential disc with a central bulge. The profiles have been fitted (dashed lines) with an exponential outside of 7 kpc. The resulting scale-lengths r_h are given in the legends.

The two different galaxies show a range of scale-lengths. The g5664 models are all shorter than the g1536 realizations. The WDM5 model of g5664 reports a particularly short scale-length because its surface brightness profile has a flat feature at approximately 6 kpc, and then a sharp break outside that. Since the exponential was only fitted outside 7 kpc it results in a steep scale length.

At $z = 0$, the time at which the profiles are shown, the galaxy g5664 is in the process of accreting a satellite. The exact timing of the merger varies between the WDM models. The flat feature in the B -band surface brightness profile in the WDM5 and WDM2 models results from the tidal inter-

action with the satellite, while the ‘bump’ at approximately 13 kpc in the WDM1 model is the satellite itself.

The surface brightness serves as a tracer of mass, so it is no surprise that the surface brightness profiles roughly follow the same trend with m_{WDM} as the total stellar mass and rotation curves of the halo: models with less stellar mass have less bright centres and less centrally peaked rotation curves. This supports the conclusion drawn from the rotation curves that the major differences in stellar abundance among the different DM models occur in the galaxies’ centres.

3.1.3 Mass accretion evolution

Since the SFH is known to have a significant impact on the evolution of the galaxies, we investigate how gas is supplied to the disc out of which those stars form. Fig. 7 shows the cumulative mass evolution of the various components of the baryonic matter along with the SFH (bottom row). The left- and right-hand columns show results for g1536 and g5664, respectively. The evolution of the total mass of baryons is shown in the top row, stellar mass evolution is shown in the second row and gas evolution is shown in the third row. Solid lines show the mass contained within the virial radius, while the dashed lines show the mass in a disc that is 6 comoving kpc thick with a radius of 20 comoving kpc (dashed lines). The disc volume was aligned based on the angular momentum of gas inside 3 kpc of the respective halo. The bottom panel shows the SFH of all stars bound in the $z = 0$ halo.

Merging events (i. e. the time at which a satellite enters the virial radius) are apparent as sudden increases in the total baryonic mass. The arrows in the top panel of Fig. 7 indicate an average time when the last significant satellite

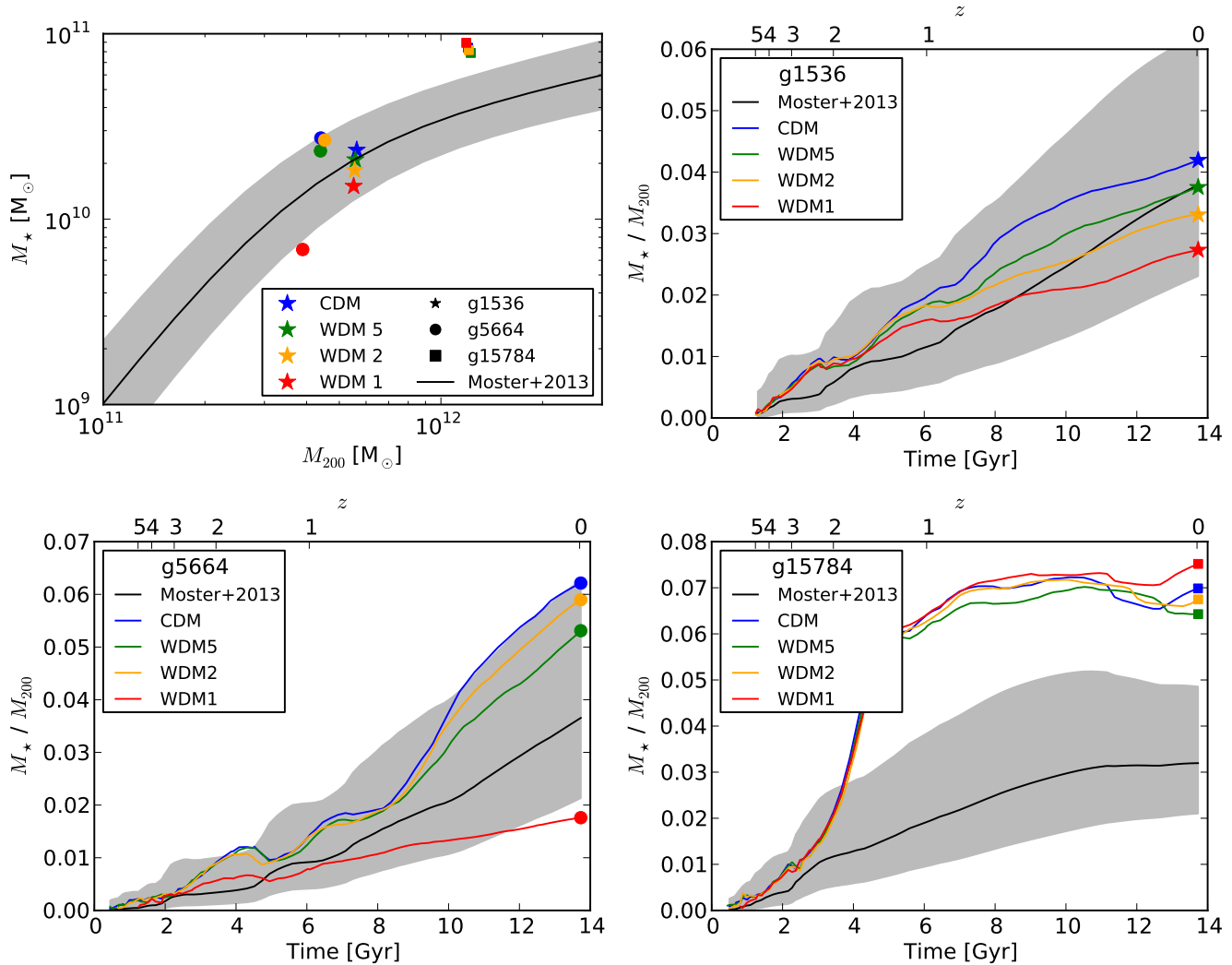


Figure 4. Stellar mass–halo mass relation of the simulated galaxies. The upper left panel shows the stellar mass of all simulated galaxies as a function of total halo mass at $z = 0$. The other panels show the evolution of the stellar mass–halo mass ratio as a function of cosmic time for each galaxy (upper right: g1536, lower left: g5664, lower right: g15784). The black lines visualize observational results obtained from abundance matching (Moster et al. 2013) and the shaded area represents the corresponding 1σ scatter. While all implementations of g1536 and g5664 ($M_{\text{halo}} < 10^{12}M_{\odot}$) roughly match observational results all simulations of g15784 ($M_{\text{halo}} > 10^{12}M_{\odot}$) produce too many stars.

crossed the virial radius in the different DM models.¹ The satellite accreted in the WDM1 model of the galaxy g5664 has about half the mass of the corresponding satellite that is accreted in the other DM models. The lower satellite mass results in the reduced SF shown in the WDM1 model of g5664 in Fig. 4. The vertical dashed lines in Fig. 7 indicate the onset of star ‘bursts’ in the two CDM models.

The onset of the most prominent SF feature in g1536 ($t \approx 6.5$ Gyr, second vertical dashed line) occurs just after this last merging event. After that merging event, the stellar mass evolution of the various models separate such that the increase in SF is larger for more massive particle candidates. Over the course of the next 4 Gyr, the SF rates in the models

that saw the greatest increase in SF gradually decrease back to the same SF rate as the models that saw no increase in SF.

The top panel shows that all the models gain baryonic mass at nearly identical rates with the slight exception that the WDM1 halo has more baryons before and until 2 Gyr after the merger at which point the baryon content of the other models surpasses WDM1. Thus, the reduced stellar mass in the WDM1 model cannot be explained as a simple, straightforward result of less baryons leading to less SF. Instead, the cause of the SF event must be more subtle for g1536. The evolution of the baryonic content of the disc of g1536 shows exactly the same trend as SF and hence stellar mass. Partly, this is due to the fact that more SF leaves more stars in the disc, but the evolution of the disc gas mass shown in the third panel shows that while all the discs contain about the same amount of mass (note the different

¹ The arrow indicates the average between the earliest and the latest merging time. These extreme times are < 200 Myr from the time indicated by the arrow

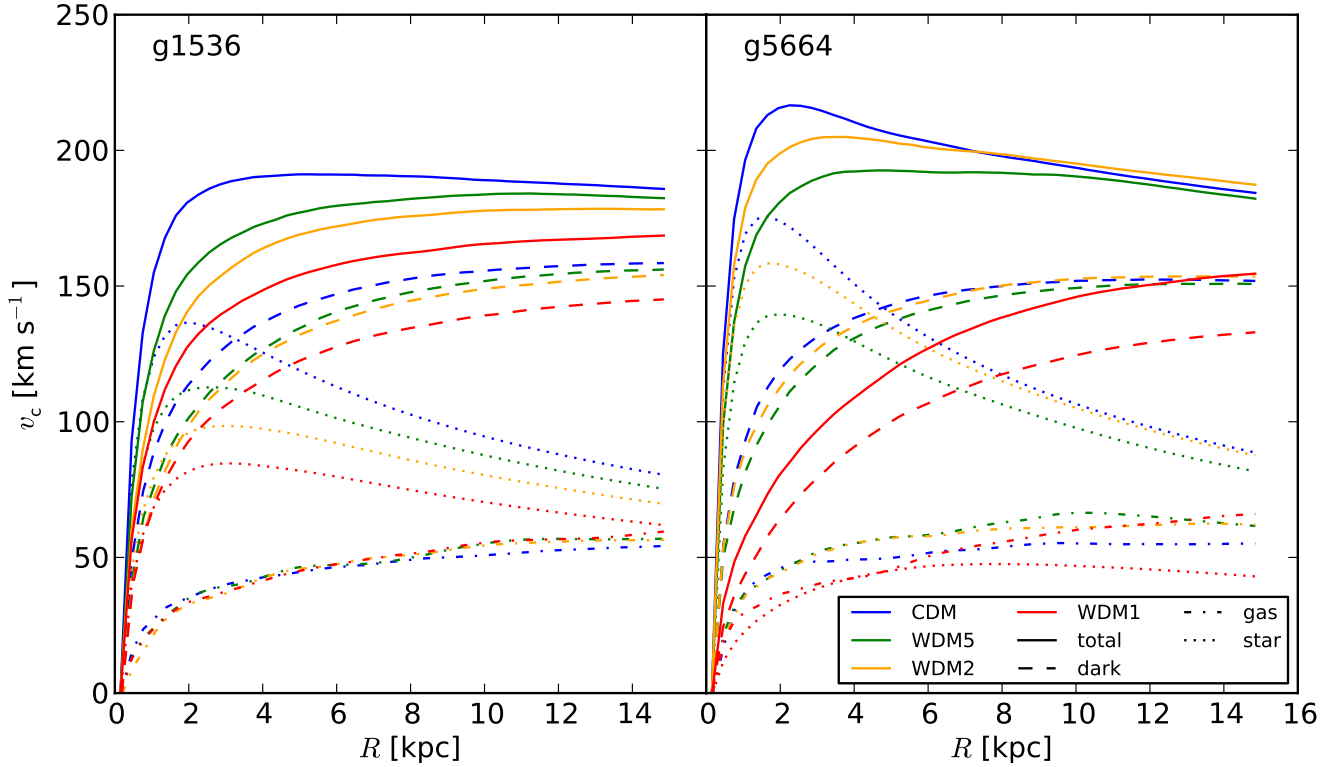


Figure 5. Partial rotation curves of the hydrodynamic simulations of g1536 (left-hand panel) and g5664 (right-hand panel). The plot shows the circular velocity $v_c = \sqrt{GM(<R)/R}$ as a function of R . The solid lines represent the total rotation curves, the dashed, dash-dotted and dotted lines the contributions of DM, gas and stellar mass, respectively.

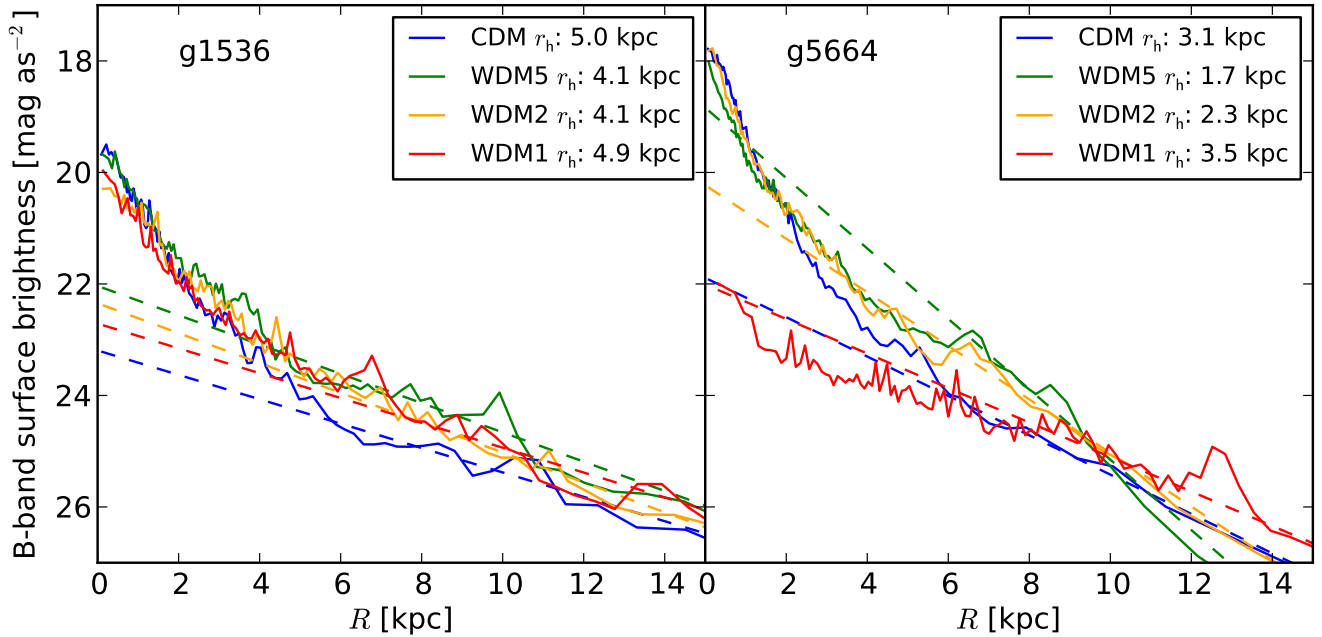


Figure 6. B-band surface brightness profiles of g1536 (left-hand panel) and g5664 (right-hand panel). The solid lines show the inferred surface brightness profiles, the dashed lines show the result of exponential fits to the profiles for $R > 7$ kpc. Except for the WDM model of g5664, all galaxies feature a central bulge. It is less pronounced for warmer DM models in the case of g1536.

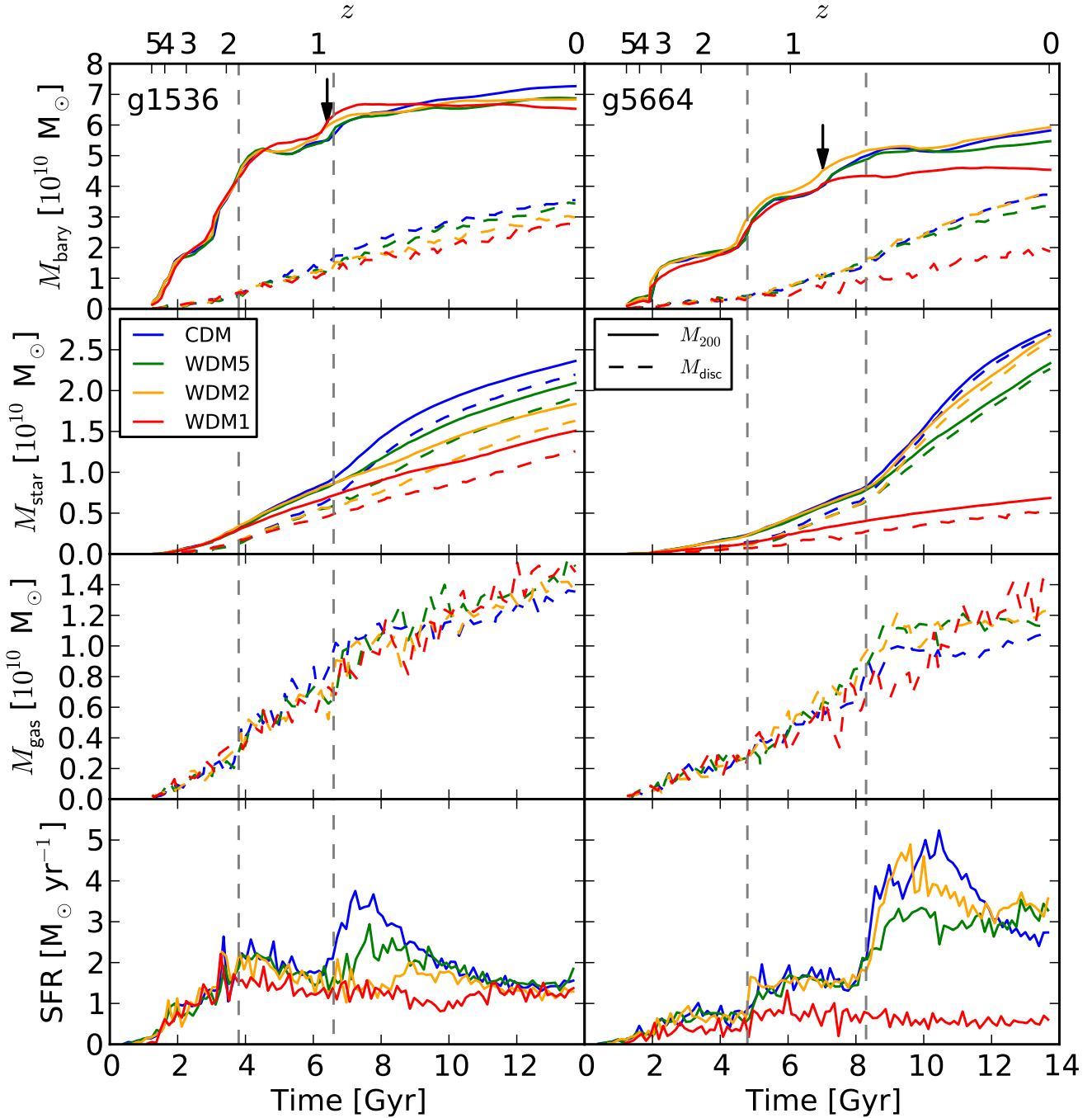


Figure 7. Accretion histories of baryons and SFH for g1536 and g5664. The plots show the evolution of baryonic (upper row), stellar (second row) and gas (third row) mass of the simulated galaxies’ main progenitor. The bottom row shows the SFH of the galaxy. The left-/right-hand panels represent the results for g1536/g5664. Solid lines represent all mass within the virial radius and the dashed lines represent all mass that is closer than 3 comoving kpc to the plane of the disc and 20 comoving kpc to the disc’s rotational axis. The gas mass of the entire halo is not shown. Sudden increases in baryonic mass (upper panels) indicate merging events with satellite galaxies. The vertical dashed lines are a guide for the eye and indicate those points in time at which enhanced SF occurs in the CDM models. The arrows indicate the time of the last significant merger. In each of the DM models, this merger happens within ± 200 Myr around the time, marked by the arrow.

scales for each panel), the CDM model generally contains more until well after the merger when the SF is more efficient, so SF consumes the gas and the total gas content drops below the other models.

Contrary to g1536, the WDM1 model of g5664 shows a large discrepancy in total baryonic mass from the other models following a merger at $z \sim 1$. The discrepancy leads directly to much less SF. Regarding the baryonic mass content of the disc, the different m_{WDM} models for g5664 do not line up sequentially according to WDM candidate mass. However, as in g1536, the stellar mass of the disc follows the baryonic mass of the disc. Thus, the SFH most clearly correlates with the mass of baryons in the disc of the galaxy, which is the result of how efficiently gas is accreted on to the disc. Once the gas is accreted to the disc it reaches densities where it can form stars. The correlation between stellar and baryonic mass in the disc is less pronounced but also evident after the merging events preceding the first vertical dashed line in Fig. 7 for both galaxies.

3.2 The effects of merging

Significant differences in SF (indicated by the vertical dashed lines in Fig. 7) occur just after merging events (indicated by increases in total baryonic mass in Fig. 7). For both galaxies studied, we saw that the efficiency of SF correlates to the baryonic mass of the disc. We now take a closer look at how the differences in the WDM models can have different effects on the disc. Each model has nearly the same merger history, but because of the changes to the initial power spectrum inherent in our WDM model, the satellites that merge have slightly different properties. We find that the way these satellites evolve changes the metal content of the halo and the magnitude of disc instabilities excited in the disc, both of which lead to changes in the SFH.

This difference in the satellites' properties is not surprising. The effect of WDM on structure formation becomes stronger when the halo mass approaches the cut-off scale in the power spectrum (e.g. Bode et al. 2001; Schneider et al. 2012; Kang et al. 2013). The satellites we discuss in this section have a mass of $\approx 10^{10} M_{\odot}$ and hence they are more sensitive to the effects of the WDM component.

3.2.1 Disc instabilities

Dynamical instabilities in discs collapse gas to higher densities. Discs collapse due to instability when the potential determined by their surface density (Σ) is too great for their velocity dispersion and their epicyclic frequency (κ) to support. Thus, as discs grow in mass, they become more prone to unstable collapse. Such collapse can create high density regions in which stars can form more efficiently. Interactions with satellites can also drive instabilities in the disc (Mihos & Hernquist 1996).

The top panels of Fig. 8 show that at the time of the SF increase associated with the second merger (right grey dashed line) there is a dramatic rise in the quantity of dense ($n > n_{\text{th}}$) gas in the CDM simulation. There is progressively less dense gas in warmer DM candidates in the case of g1536 (left). The increase in dense gas suggests that the tidal interaction with the accreting satellite in the CDM model is

effective at driving instabilities to increase SF. In the case of g5664 (right) the coincidence of the onset of SF and the excess of dense gas in the disc is also evident. However, we do not see the trend with warmer DM which is consistent with what we saw in stellar mass evolution and SFH (cf. Fig. 7). Note that the delay between the merging event and the corresponding star formation feature is much longer for g5664 compared to g1536. This is due to the satellites' orbits. While the satellite of g1536 falls straight into the centre of the host galaxy the satellite of g5664 has a more tangential orbit and approaches the host's centre much slower. Thus, its effects on the host's disc are delayed more.

3.2.2 Gas halo metal enrichment

The bottom panels of Fig. 8 show the evolution of the metallicity in the gas disc (dashed lines) and the gas halo outside the disc (solid lines) for all the WDM models in g1536 (left-hand panel) and g5664 (right-hand panel). Elements with atomic masses higher than hydrogen and helium are produced through fusion reactions inside stars, with the most massive elements forming in massive stars that have evolved off the stellar main sequence and started fusing elements heavier than hydrogen and helium. When these stars explode as SNe, the metals leave the star as part of a hot ($> 10^6$ K) gas phase that has enough energy to leave the disc potential. Some of the metals mix into the interstellar medium gas that comprises the disc, increasing the disc gas metallicity, as shown in Fig. 8. The rest of the metals leave the disc to create and enrich the hot gas halo.

Stars formed in satellites also create metals. Since the satellites in our models have lower mass than the main disc, their gravitational potential is shallower, so it is easier for the hot gas to leave the satellites.

The most significant difference in metal content of the gaseous haloes in the g1536 models happens after the first grey dashed line at 4.2 Gyr. We see in the simulations that there are three minor satellites accreting on to the disc at this time. The three satellites have reasonably similar properties in the CDM, WDM5 and WDM2 models, but have many fewer stars and less dense gas in the WDM1 model. The satellites that have formed a few stars when they enter the halo bring cool, metal poor gas into what is already a metal enriched main halo. The cool gas is not ram-pressure stripped initially because the depth of the satellite potential well is too deep. As the satellites reach the pericentre of their orbit, they are tidally stirred (Mayer et al. 2001) and develop dense gas regions. These dense regions form stars and blow out hot, metal-enriched gas much more efficiently than the satellites had previously. The difference in halo metallicity between the WDM1 model, in which the satellites were too tenuous to form stars, and the other models in which stars form is clear in Fig. 8. This low efficiency of SF in the WDM1 satellites is due to a combination of their later formation time (e.g. Macciò & Fontanot 2010a) and due to their reduced central concentration (e.g. Schneider et al. 2012).

For the g5664 galaxy, the situation is similar. The halo metallicity in the WDM1 model is lower than that of the other DM models. However, here this difference occurs before the first major onset of SF, i.e. even at the highest redshifts at which we were able to identify the galaxy's main

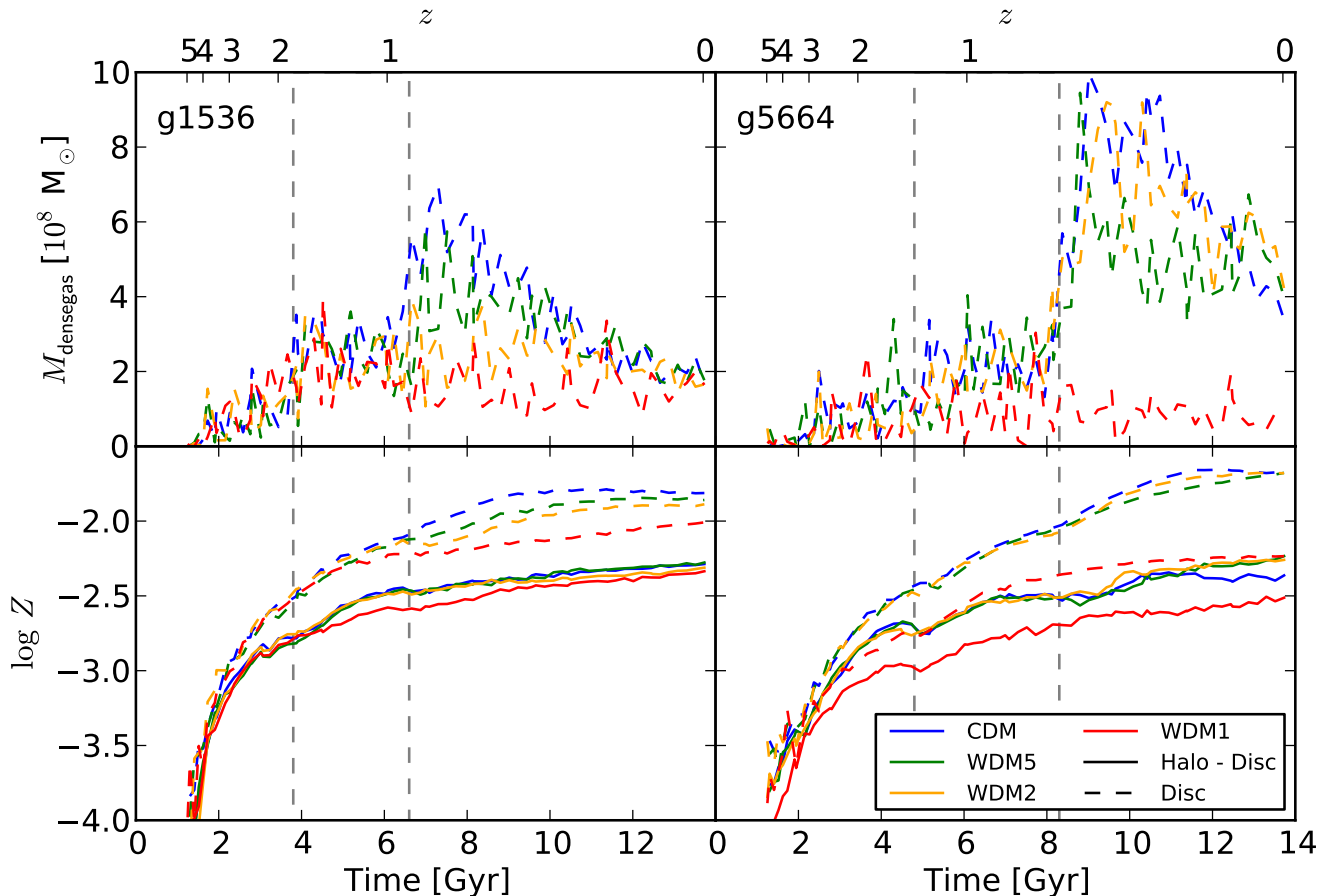


Figure 8. Evolution of the dense gas mass (top row) and metallicity (bottom row) of the gas in g1536 (left) and g5664 (right). The dashed lines show the dense gas mass and metallicity of the gas in the disc (6 comoving kpc thick and 20 comoving kpc radius) and the solid lines in the bottom panels show the metallicity for all the gas in the halo without the disc. The vertical dashed lines are the same as in Fig. 7, i. e. they indicate the onset of major star formation effects.

progenitor. This indicates that SF in the WDM1 model of g5664 stays behind compared to colder DM models due to delayed halo formation in warmer DM.

The difference in halo metallicity between the WDM1 and the other DM models decreases at late times since the metal enriched gas can escape from the disc in the WDM1 model more easily due to its shallower potential well.

The result of the increased metallicity in the gas halo is that the cooling rate increases. Thus, gas cools quicker out of the halo on to the disc. As we have seen, more gas in the disc leads to more SF.

3.3 WDM versus stellar feedback

§3.1 illustrated how the nature of DM can have an effect on the morphology of disc galaxies. It is interesting to compare these effects with the influence of baryonic physics on the process of galaxy formation. In order to test this, a second series of simulations using the most extreme WDM model (WDM1) was carried out with a variety of ESF efficiencies, c_{ESF} , from none to the fiducial value. The evolution of the stellar mass–halo mass ratio for these simulations is presented in Fig. 9. The results reflect what was found in Stinson et al. (2013a): ESF effectively delays SF. Even us-

ing the most extreme WDM model, too many stars form early with the slightest reduction of c_{ESF} . Simulations with $c_{\text{ESF}} \lesssim 0.075$ form too many stars at high z . One interesting trend is apparent: The simulations without ESF form less stars by $z = 0$ than some simulations with a small amount of ESF. The final stellar mass is lower without ESF because gas collapses to higher densities without ESF, which causes more intense starbursts that drive stronger outflows. These outflows remove large amounts of gas leading to a lack of SF fuel at later times which leads to the suppressed SF at $z \lesssim 2$. This effect has been described by Stinson et al. (2013a) in CDM and applies to galaxy formation in WDM models as well. The fact that it occurs in the most extreme case of the explored WDM models shows that the effects of WDM are minimal compared to baryonic feedback processes.

4 CONCLUSIONS

We carried out a series of hydrodynamical cosmological zoom simulations of the formation of three different galaxies. Each galaxy was simulated in four different DM models ranging from the standard CDM scenario to WDM models with a DM candidate mass as low as $m_{\text{WDM}} = 1 \text{ keV}$.

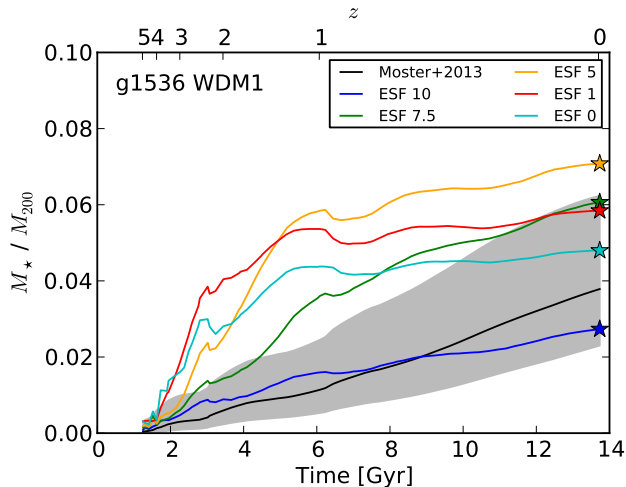


Figure 9. Evolution of the stellar mass–halo mass ratio for simulations of g1536 WDM1 with different ESF efficiencies.

Galaxy formation proceeded in a similar fashion regardless of the WDM model used. Overall WDM reduces the SF rate, which results in a marginally lower total stellar mass at $z = 0$ and in less centrally concentrated stellar profiles.

We find that these differences are mainly due to the different properties of the few satellites merging with the central object. In the CDM model satellite interactions triggered disc instabilities that drove gas to the centre where it greatly increased the rate of SF and consequently raised the rotation curve in the centre. In some cases, the increase in SF was simply due to the creation of dense gas in the tidal interaction with the satellite. In other cases, the increase in SF could be traced to metals ejected from the satellites into the gas surrounding the main disc. The metal-enriched halo proceeded to cool faster on to the disc, which increased SF.

While the CDM and the WDM galaxies share the same merger histories the properties of the incoming satellites differed from model to model, most significantly between the extremes of our simulations, the coldest, CDM, and warmest, WDM1, models. Due to the later formation time and the reduced DM concentration of the WDM1 satellites that are predicted in several N -body studies (e.g. Schneider et al. 2012) the satellites in the warmest model were least efficient in retaining their gas and forming stars. As a consequence they had the least (hydro)dynamical impact on the central object during the merging phase, and did not trigger any bursts of SF.

The reduced impact of satellites in the WDM1 model is mostly notable in the galactic rotation curves, which are indeed rising much slower than in the CDM simulations.

However, this effect could be matched with minor variations of the stellar feedback. The series of tests simulated with a variation of the ESF (feedback from massive stars before they explode as SN) showed that the feedback had a stronger effect than the difference between CDM and the warmest, 1 keV WDM1 model.

A clear signature of the effects of a WDM component was only seen in two out of the three simulated galaxies. The effects only appeared in galaxies that had realistic properties like stellar mass–halo mass ratio and a realistic rotation

curve. The third galaxy (due to its higher mass) was too overcooled to produce any of the observed galaxy scaling relations. In this third galaxy, the effects of WDM were erased by the unrealistically high SFE. These results again stress the need for *realistic* hydrodynamical simulations to assess the effect of cosmology on galaxy properties (e.g. Casarini et al. 2011; van Daalen et al. 2011).

Finally, the only WDM model to show a clear impact on galaxy properties was the WDM1 model. This model falls outside the current constraints on WDM particle mass. If the new limits by Viel et al. (2013) (WDM candidate masses below 3.3 keV ruled out at a confidence level of 2σ) can be confirmed, our simulations show that the effect of WDM on disc galaxy formation is minimal (if not totally absent) especially when compared to processes such as stellar feedback.

ACKNOWLEDGEMENTS

The analysis was performed using the PYNBODY package (<http://code.google.com/p/pynbody>), which had key contributions from Andrew Pontzen and Rok Roškar in addition to the authors. The simulations were performed on the THEO cluster of the Max-Planck-Institut für Astronomie at the Rechenzentrum in Garching; the clusters hosted on SHARCNET, part of ComputeCanada; the Universe cluster that is part of the COSMOS Consortium at Cambridge, UK; the HPCAVF cluster at the University of Central Lancashire; and the Milky Way supercomputer, funded by the Deutsche Forschungsgemeinschaft (DFG) through Collaborative Research Center (SFB 881) ‘The Milky Way System’ (subproject Z2), hosted and co-funded by the Jülich Supercomputing Center (JSC). We greatly appreciate the contributions of all these computing allocations. AVM and GSS acknowledge support through the Sonderforschungsbereich SFB 881 ‘The Milky Way System’ (subproject A1) of the German Research Foundation (DFG). CB acknowledges Max-Planck-Institut für Astronomie for its hospitality and financial support through the Sonderforschungsbereich SFB 881 ‘The Milky Way System’ (subproject A1) of the German Research Foundation (DFG). HMPC and JW gratefully acknowledge the support of NSERC. HMPC also appreciates the support he received from CIFAR.

REFERENCES

- Abazajian K., Koushiappas S. M., 2006, *Phys. Rev. D*, 74, 023527
- Agertz O., Teyssier R., Moore B., 2011, *MNRAS*, 410, 1391
- Alongi M., Bertelli G., Bressan A., Chiosi C., Fagotto F., Greggio L., Nasi E., 1993, *A&AS*, 97, 851
- Anderhalden D., Schneider A., Macciò A. V., Diemand J., Bertone G., 2013, *J. Cosmol. Astropart. Phys.*, 3, 14
- Bode P., Ostriker J. P., Turok N., 2001, *ApJ*, 556, 93
- Boyarsky A., Lesgourgues J., Ruchayskiy O., Viel M., 2009a, *J. Cosmol. Astropart. Phys.*, 5, 12
- Boyarsky A., Ruchayskiy O., Iakubovskiy D., 2009b, *J. Cosmol. Astropart. Phys.*, 3, 5
- Boylan-Kolchin M., Bullock J. S., Kaplinghat M., 2011, *MNRAS*, 415, L40

- Bressan A., Fagotto F., Bertelli G., Chiosi C., 1993, *A&AS*, 100, 647
- Brook C. B., Stinson G., Gibson B. K., Wadsley J., Quinn T., 2012, *MNRAS*, 424, 1275
- Bullock J. S., Kravtsov A. V., Weinberg D. H., 2000, *ApJ*, 539, 517
- Casarini L., Macciò A. V., Bonometto S. A., Stinson G. S., 2011, *MNRAS*, 412, 911
- Chabrier G., 2003, *PASP*, 115, 763
- Colín P., Avila-Reese V., Valenzuela O., 2000, *ApJ*, 542, 622
- Colombi S., Dodelson S., Widrow L. M., 1996, *ApJ*, 458, 1
- Di Cintio A., Brook C. B., Macciò A. V., Stinson G. S., Knebe A., Dutton A. A., Wadsley J., 2013, arXiv:1306.0898
- Diemand J., Moore B., Stadel J., 2004, *MNRAS*, 352, 535
- Efstathiou G., 1992, *MNRAS*, 256, 43P
- Font A. S. et al., 2011, *MNRAS*, 417, 1260
- Gao L., Theuns T., 2007, *Science*, 317, 1527
- Garrison-Kimmel S., Rocha M., Boylan-Kolchin M., Bullock J. S., Lally J., 2013, *MNRAS*
- Governato F., Willman B., Mayer L., Brooks A., Stinson G., Valenzuela O., Wadsley J., Quinn T., 2007, *MNRAS*, 374, 1479
- Guedes J., Callegari S., Madau P., Mayer L., 2011, *ApJ*, 742, 76
- Hansen S. H., Lesgourgues J., Pastor S., Silk J., 2002, *MNRAS*, 333, 544
- Jonsson P., 2006, *MNRAS*, 372, 2
- Kang X., Macciò A. V., Dutton A. A., 2013, *ApJ*, 767, 22
- Kannan R., Stinson G. S., Macciò A. V., Brook C., Weinmann S. M., Wadsley J., Couchman H. M. P., 2013, arXiv:1302.2618
- Katz N., 1992, *ApJ*, 391, 502
- Kennicutt Jr. R. C., 1998, *ApJ*, 498, 541
- Khlopov M. Y., Kouvaris C., 2008, *Phys. Rev. D*, 78, 065040
- Khlopov M. Y., Stephan C. A., 2005, astro-ph/0511796
- Klypin A., Kravtsov A. V., Valenzuela O., Prada F., 1999, *ApJ*, 522, 82
- Knebe A., Devriendt J. E. G., Mahmood A., Silk J., 2002, *MNRAS*, 329, 813
- Knollmann S. R., Knebe A., 2009, *ApJS*, 182, 608
- Koposov S. E., Yoo J., Rix H.-W., Weinberg D. H., Macciò A. V., Escudé J. M., 2009, *ApJ*, 696, 2179
- Kuzio de Naray R., Martinez G. D., Bullock J. S., Kaplinghat M., 2010, *ApJ*, 710, L161
- Lopez L. A., Krumholz M. R., Bolatto A. D., Prochaska J. X., Ramirez-Ruiz E., 2011, *ApJ*, 731, 91
- Lovell M. R. et al., 2012, *MNRAS*, 420, 2318
- Lupton R., Blanton M. R., Fekete G., Hogg D. W., O'Mullane W., Szalay A., Wherry N., 2004, *PASP*, 116, 133
- Macciò A. V., Fontanot F., 2010a, *MNRAS*, 404, L16
- Macciò A. V., Kang X., Fontanot F., Somerville R. S., Koposov S., Monaco P., 2010b, *MNRAS*, 402, 1995
- Macciò A. V., Paduroiu S., Anderhalden D., Schneider A., Moore B., 2012a, *MNRAS*, 424, 1105
- Macciò A. V., Stinson G., Brook C. B., Wadsley J., Couchman H. M. P., Shen S., Gibson B. K., Quinn T., 2012b, *ApJ*, 744, L9
- Macciò A. V., Ruchayskiy O., Boyarsky A., Muñoz-Cuartas J. C., 2013, *MNRAS*, 428, 882
- Marinacci F., Pakmor R., Springel V., 2013, arXiv:1305.5360
- Mayer L., Governato F., Colpi M., Moore B., Quinn T., Wadsley J., Stadel J., Lake G., 2001, *ApJ*, 559, 754
- Menci N., Fiore F., Lamastra A., 2012, *MNRAS*, 421, 2384
- Menci N., Fiore F., Lamastra A., 2013, *ApJ*, 766, 110
- Mihos J. C., Hernquist L., 1996, *ApJ*, 464, 641
- Miranda M., Macciò A. V., 2007, *MNRAS*, 382, 1225
- Moore B., Ghigna S., Governato F., Lake G., Quinn T., Stadel J., Tozzi P., 1999, *ApJ*, 524, L19
- Moster B. P., Naab T., White S. D. M., 2013, *MNRAS*, 428, 3121
- Moster B. P., Somerville R. S., Maubetsch C., van den Bosch F. C., Macciò A. V., Naab T., Oser L., 2010, *ApJ*, 710, 903
- Narayanan V. K., Spergel D. N., Davé R., Ma C.-P., 2000, *ApJ*, 543, L103
- Nickerson S., Stinson G., Couchman H. M. P., Bailin J., Wadsley J., 2011, *MNRAS*, 415, 257
- Okamoto T., Frenk C. S., 2009, *MNRAS*, 399, L174
- Pellegrini E. W. et al., 2007, *ApJ*, 658, 1119
- Power C., Navarro J. F., Jenkins A., Frenk C. S., White S. D. M., Springel V., Stadel J., Quinn T., 2003, *MNRAS*, 338, 14
- Quinn T., Katz N., Efstathiou G., 1996, *MNRAS*, 278, L49
- Robertson B., Bullock J. S., Cox T. J., Di Matteo T., Hernquist L., Springel V., Yoshida N., 2006, *ApJ*, 645, 986
- Scannapieco C. et al., 2012, *MNRAS*, 423, 1726
- Schneider A., Smith R. E., Macciò A. V., Moore B., 2012, *MNRAS*, 424, 684
- Seljak U., Makarov A., McDonald P., Trac H., 2006, *Phys. Rev. Lett.*, 97, 191303
- Somerville R. S., 2002, *ApJ*, 572, L23
- Spergel D. N. et al., 2007, *ApJS*, 170, 377
- Springel V. et al., 2008, *MNRAS*, 391, 1685
- Springel V. et al., 2005, *Nature*, 435, 629
- Stinson G., Seth A., Katz N., Wadsley J., Governato F., Quinn T., 2006, *MNRAS*, 373, 1074
- Stinson G. S., Bailin J., Couchman H., Wadsley J., Shen S., Nickerson S., Brook C., Quinn T., 2010, *MNRAS*, 408, 812
- Stinson G. S. et al., 2012, *MNRAS*, 425, 1270
- Stinson G. S., Brook C., Macciò A. V., Wadsley J., Quinn T. R., Couchman H. M. P., 2013a, *MNRAS*, 428, 129
- Stinson G. S. et al., 2013b, *MNRAS*, 436, 625
- van Daalen M. P., Schaye J., Booth C. M., Dalla Vecchia C., 2011, *MNRAS*, 415, 3649
- Viel M., Becker G. D., Bolton J. S., Haehnelt M. G., 2013, *Phys. Rev. D*, 88, 043502
- Viel M., Becker G. D., Bolton J. S., Haehnelt M. G., Rauch M., Sargent W. L. W., 2008, *Phys. Rev. Lett.*, 100, 041304
- Viel M., Lesgourgues J., Haehnelt M. G., Matarrese S., Riotto A., 2005, *Phys. Rev. D*, 71, 063534
- Viel M., Lesgourgues J., Haehnelt M. G., Matarrese S., Riotto A., 2006, *Phys. Rev. Lett.*, 97, 071301
- Wadsley J. W., Stadel J., Quinn T., 2004, *New Astron.*, 9, 137
- Zolotov A. et al., 2012, *ApJ*, 761, 71